ACS OMEGA

http://pubs.acs.org/journal/acsodf

Article

Effect of Vacuum-Sealed Annealing and Ice-Water Quenching on the Structure and Photocatalytic Acetone Oxidations of Nano-TiO_2 Materials

Liping Wen, Yao Liu, Yong Liu, Yuping Xu, and Baoshun Liu*

Cite This: *ACS Omega* 2022, 7, 43710–43718

Read Online

ACCESS | Metrics & More | Article Recommendations

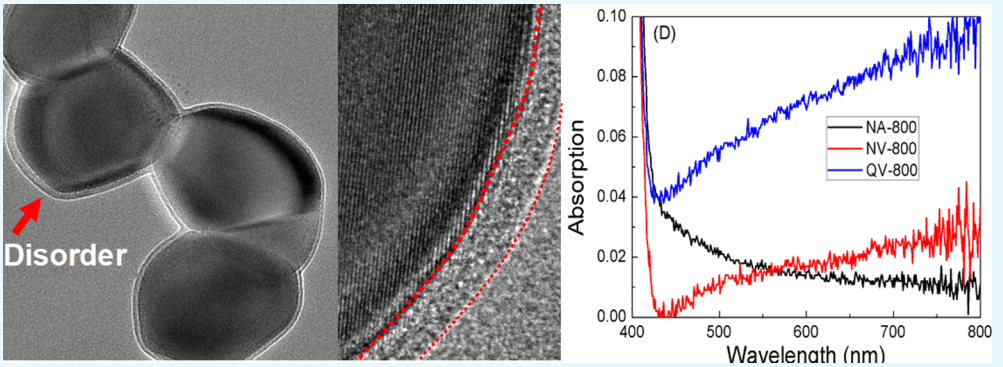

ABSTRACT: In the current research, P25 TiO_2 materials sealed in quartz vacuum tubes were subject to annealing and ice-water post-quenching, with the effects on TiO_2 structures, morphology, and photocatalytic activity being studied. It is shown that the vacuum-sealed annealing can lead to a decrease in the crystallinity and temperature of anatase-to-rutile phase transition. A disorder layer is formed over TiO_2 nanoparticles, and the TiO_2 lattices are distorted between the disorder layer and crystalline core. The ice-water post-quenching almost has no effect on the crystalline structure and morphology of TiO_2. It can be seen that the vacuum-sealed annealing can generate more defects, and the electrons are mainly localized at lattice Ti sites, as well as the percentage of bulk oxygen defects is also increased. Although further ice-water post-quenching can introduce more defects in TiO_2, it does not affect the electron localization and defect distribution. The vacuum-sealed annealing process can increase the photocatalytic acetone oxidations of the anatase phase TiO_2 to some extent, possibly because of the defect generation and Ti^{3+} site formation; the further ice-water quenching leads to a decrease in the photocatalytic activity because more defects are introduced.

1. INTRODUCTION

Defect engineering is a main strategy to modify the photocatalytic properties of semiconductors.[1−3] It had been reported that both the native and extrinsic defects can play a major role in photocatalytic reactions for many materials,[4−6] such as volatile organic compound removal and polluted water treatment.[7,8] As a prototype of photocatalytic materials, the effect of defects for TiO_2 materials on their photocatalytic properties has been widely studied.[9−15] It was found that defects can result in intermediate gap states under a synergism with lattice Ti atoms;[16−18] this can alter the charge carrier kinetics and photocatalytic activities.[19−21] Therefore, defect physics and chemistry are important and meaningful for TiO_2 photocatalysis.

The role of defects depends on their location in the TiO_2 lattice. Bulk defects cannot affect charge carrier transfer as they are separated from photocatalytic reactants, so it is considered that they generally form recombination centers and are harmful to photocatalysis. Surface defects are able to change charge carrier transfer to reactants, so the photocatalytic property could be increased. For example, many studies had reported that surface oxygen defects can increase the photocatalytic activities;[22−24] It had also been shown that bulk oxygen defects can cooperate with surface oxygen defects in photocatalytic reactions.[25,26] The self-dopants, Ti^{3+} ions, cannot be formed in native TiO_2. More Ti^{3+} states can be generated in reduced environments for responding to visible light;[27−30] it had also been reported that bulk Ti^{3+} sites might increase the charge carrier mobility, and surface Ti^{3+} states are dynamically formed

Received: July 25, 2022
Accepted: November 2, 2022
Published: November 17, 2022

https://doi.org/10.1021/acsomega.2c04695
ACS Omega 2022, 7, 43710−43718

and can shuttle electron transfer to generate H_2.[31] Zhang et al. proposed a strategy to increase the thermal activation of the trapped electrons out of deep-level defects by introducing shallow defects. They showed that the incorporation of hydrogen dopants into TiO_2 lattices can form shallow-level defects above the deep oxygen vacancies, and it was seen that the solar light-induced CO_2 reduction and UV light-induced acetaldehyde removal can be greatly increased.[32] It is also found that the disordered layer, which can also be considered as a kind of defect that is located over surfaces, is meaningful in increasing the photocatalytic properties. In a study performed by Zhang et al., high-powered ultrasonic treatment was used to generate a disorder layer over TiO_2, which also promoted the high-dispersion Pt nanoparticles over surfaces; the obtained Pt/TiO_2 shows highly photothermal CH_4 formation during CO_2 reduction.[33]

The native defects are very low in intrinsic TiO_2, so many methods, such as chemical reduction, vacuum annealing, Ar^+ ion sputtering, and high-energy electron bombardment, were used to create extra defects.[25,34,35] Different methods could lead to different kinds of defects, and their effect on TiO_2 photocatalytic activity might also be different. From this viewpoint, developing a new defect formation method and studying the role in photocatalysis are still attractive for TiO_2 and other materials. Recently, ice-water[36] and liquid-N_2[37] quenching were used by us to create defects in TiO_2, and it was seen that the photocatalytic activities can be increased to some extent. The present research studied the effect of the vacuum-sealed annealing and the post ice-water quenching on the defects of TiO_2, and the effects on structure and morphology were also investigated. It was found that the photocatalytic activity of the anatase TiO_2 was increased to some extent by the vacuum-sealed annealing, which is however decreased after ice-water post-quenching.

2. EXPERIMENTAL SECTION

2.1. Sample Preparation. Commercial P25 TiO_2 was used as the source material without further treatment. As shown in Figure 1, 0.5 g of TiO_2 was first placed in a bottom-sealed quartz glass tube and was then connected to a vacuum pump. Oxyhydrogen flame was used to seal the quartz tube during continuous vacuum evacuation. The sealed samples were then annealed at different temperatures for 2 h. Just after annealing, the samples were directly thrown into ice water for quenching. The normally cooled samples, that is, the sealed sample was kept in a furnace for slow cooling until room temperature, were also prepared for comparison. In addition, the samples that were not sealed in a quartz tube were also prepared by annealing in air and then normally cooled in furanone. The normally cooled air-annealed samples, normally cooled vacuum annealed samples, and ice-water-quenched vacuum-annealed samples pre-annealed at XXX °C are denoted as NA-TiO_2-XXX, NV-TiO_2-XXX, and QV-TiO_2-XXX, respectively.

2.2. Structural Characterization. The sample's crystallinity was checked with a D/MAX-IIIA X-ray diffraction (XRD) spectrometer in a 2θ mode and a RENISHAW Raman spectroscope equipped with an optical microscope, with the 635 nm Ar^+ ion laser line being focused with an analyzing spot of ~1 μm on the sample under the microscope for excitation. The sample images were observed with a field emission transmission electron microscope (type: JEM2100F, JEOL, Tokyo, Japan). UV−vis diffusion spectra were obtained with a UV−Vis photospectrometer in the wavelength range from 200 to 800 nm (type: UV-2600, Shimadzu, Tokyo, Japan). Surface chemical

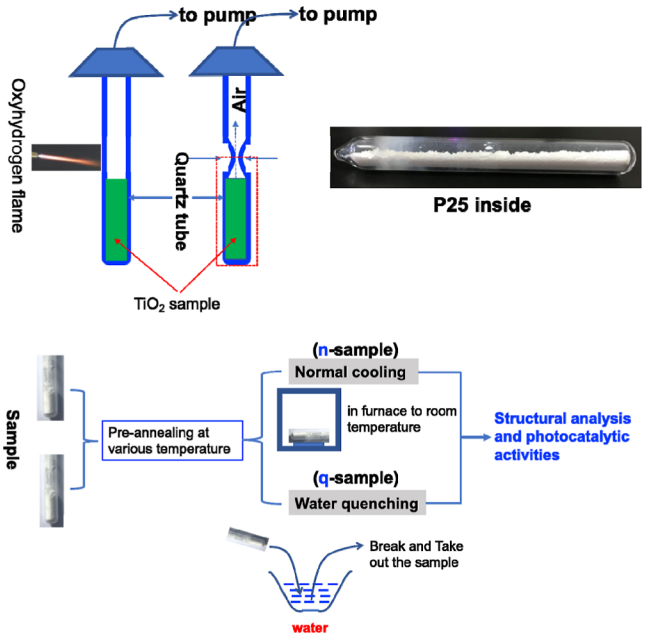

Figure 1. Schematic diagram for the vacuum sealing of TiO_2 in a quartz tube, and the procedure for the normal cooling and ice-water quenching of the vacuum-sealed TiO_2.

compositions were determined by an X-ray photoelectron spectrometer (type: VG Multilab 2000, Thermo Scientific, Waltham, America), with an Al kα radiation being used as the X-ray source, and the binding energy (284.6 eV) of C 1s electrons was used as the energy reference. The X-band electron paramagnetic resonance (EPR) spectra were recorded on a Bruker EMX spectrometer equipped with a cylindrical quart tube operating at 100 kHz field modulation and a temperature of 150 K. Positron annihilation lifetime spectra were recorded using a conventional ORTEC-583 fast−fast coincident system at room temperature to check the location of oxygen defects and their relative contents.

2.3. Photocatalytic Activity Evaluation. The photocatalytic oxidation of acetone was used to evaluate the photocatalytic activities under gaseous conditions. A self-designed reactor that can well control the light intensity and temperatures was used to conduct the experiments. A band-passed filter was equipped with a 300 W Xe lamp (PLS-SXE300, perfect light) to generate a 365 nm monochromic light. The light intensity was measured to be ~3 mW/cm^2 with a Si diode photodetector (Newport 818UV/DB). The reaction temperature was kept at 50 °C to avoid the influence of ambient temperature change. Surface temperatures were also confirmed with an IR meter (FTIR E60), and it was seen that light illumination had no effect. CO_2 evolutions were used to evaluate the photocatalytic activities. Samples (0.1 g) were dispersed in ϕ 30 glass containers with water. After drying, a thin TiO_2 coating was formed at the bottom of the container, which was used for photocatalysis. All samples were illuminated with a UV light for 1 day to remove surface carbonate contaminates. Clean air was first flowed through the reactor until the initial CO_2 concentration was lower than 20 ppm, and the relative humidity and relative $[O_2]$ were ~ zero and ~21%, respectively. Photocatalytic acetone oxidations were then carried out according to the following procedure. Liquid acetone (2 μL) was injected into the reactor, which was then placed in the dark for 80 min to allow an acetone adsorption over TiO_2 surfaces.

https://doi.org/10.1021/acsomega.2c04695
ACS Omega 2022, 7, 43710−43718

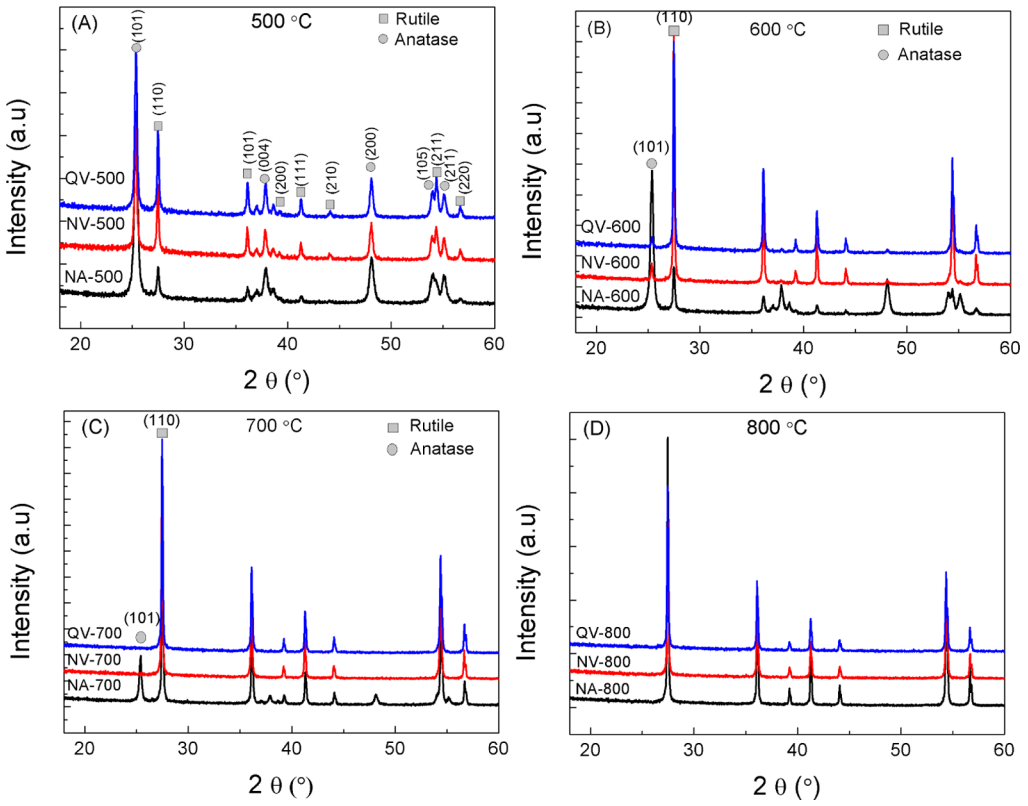

Figure 2. XRD patterns of NA-TiO_2, NV-TiO_2, and QV-TiO_2 prepared after annealing at 500 (A), 600 (B), 700 (C), and 800 °C (D), respectively.

The light was then illuminating on the samples to start photocatalytic reactions for a while. The concentrations of acetone and CO_2 were determined by a gas chromatograph (GC-2018) equipped with a Ni-based methane convertor per 5 min interval.

3. RESULTS AND DISCUSSION

3.1. Crystalline Characterization. Figure 2A–D shows the XRD patterns of NA-TiO_2, NV-TiO_2, and VQ-TiO_2 after annealing at 500, 600, 700, and 800 °C, respectively; the crystalline plane indexes are labeled to show rutile and anatase phases. It can be seen that the vacuum-sealed annealing lowers the anatase (A) to rutile (R) transition temperature by 100–150 °C. The further ice-water quenching almost has no effect on the transition temperatures and the TiO_2 crystalline structure. The promotion of A-R phase transition by vacuum-sealed annealing was also confirmed by Raman scattering spectroscopy, as shown in Figure 3A–D. We attribute the decrease of the A-R phase transition temperature to the low oxygen amounts under vacuum, which could result in more lattice defects that might play a role in catalyzing the A-to-R transition. The relative contents of rutile phase TiO_2 in the different samples were also obtained from XRD analysis and are shown in Table 1.

Figure 2D shows that all anatase TiO_2 is converted to rutile when the annealing temperature is 800 °C. The rutile crystallinity is compared with the (110) peak intensities, which shows that the refraction intensity of the NV-TiO_2 and QV-TiO_2 samples is low as compared to that of NA-TiO_2, so the vacuum-sealed annealing results in the decrease of the TiO_2 crystallinity. Figure 3 shows that the vacuum-sealed annealing has a clear effect on the Raman modes for both anatase and rutile phases. Figure 3A is normalized based on the strongest anatase Raman E_g mode at 638 cm^{-1}. In addition to the anatase vibration modes (339 cm^{-1} for the B_{1g} mode and 516 cm^{-1} for the A_{1g} mode), the E_g vibration mode of the rutile phase also appears at 446 cm^{-1}.[38] It can be seen that the anatase Raman mode at 516 cm^{-1} decreases for the vacuum-sealed annealed samples. For the samples annealed at 600 °C, the Raman spectrum of NA-TiO_2 was normalized relative to the strongest anatase peak at 638 cm^{-1}, and the Raman spectra of NV-TiO_2 and QV-TiO_2 are normalized according to the strongest rutile Raman peak at 609 cm^{-1} (A_{1g} mode). This result agrees with the XRD analysis that all anatase is converted to rutile for the vacuum-sealed samples. For the samples annealed at 700 and 800 °C, all Raman spectra are normalized based on the strongest rutile vibration mode at 609 cm^{-1}. It can be seen that the vacuum-sealed annealing leads to an increase in the E_g Raman vibration mode at 446 cm^{-1} for the rutile phase according to the unsealed samples. This Raman vibration difference indicates that a structure change is caused by vacuum-sealed annealing for both anatase and rutile phases. It is considered that the defects caused by vacuum-sealed annealing might have an effect on the Raman vibrations of TiO_2. The further ice-water quenching has no obvious effect on the Raman spectra as compared to NV-TiO_2. In addition, the Raman vibration intensities of the NV-TiO_2 and QV-TiO_2 samples are lower than that of the NA-TiO_2 samples; this also shows a decrease in crystallinity after vacuum-sealed annealing and is in good accordance with XRD analysis.

3.2. Morphological Studies. Different from direct ice-water quenching and liquid N_2 quenching,[34,35] the above results show that the vacuum-sealed annealing could change the TiO_2 crystallinity; this might also have an effect on the TiO_2 morphology. Figure 4 shows the transmission electron microscopy (TEM) and high-resolution TEM (HR-TEM) images of the untreated P25 TiO_2, NV-TiO_2-700, and NV-TiO_2-800. It can be seen from Figure 4A,B that the P25 material

https://doi.org/10.1021/acsomega.2c04695
ACS Omega 2022, 7, 43710–43718

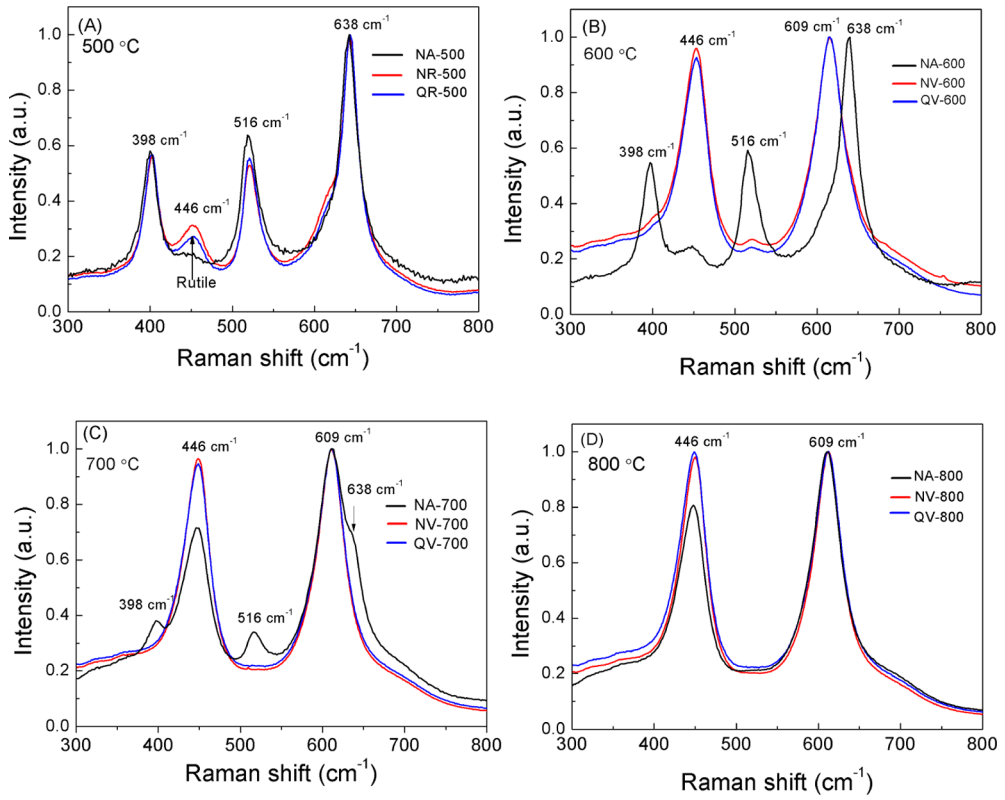

Figure 3. Raman scattering spectra of NA-TiO_2, NV-TiO_2, and QV-TiO_2 after annealing at 500 (A), 600 (B), 700 (C), and 800 °C (D), respectively.

is mainly composed of irregular nanoparticles that show the clear lattice planes of the anatase phase. The nanoparticles become larger after annealing because of the anatase-to-rutile phase transition. For NV-TiO_2-700, Figure 4C,D shows a $s \sim 4$ nm-thick disorder layer around the TiO_2 nanoparticles, and a core−shell crystalline disorder structure is formed. In addition, there is also a lattice distortion between the disorder layer and crystalline TiO_2. Figure 4E shows that the morphology of NV-TiO_2-800 is completely different from that of NV-TiO_2-700 as the crystalline core cannot be seen, and the HR-TEM image (Figure 4F) further shows that the crystalline lattice planes cannot be seen. It can be known that the formed disorder layer over the TiO_2 surface is much thicker. The surface disorder layer can reduce the crystallinity, in good accordance with the above XRD and Raman analysis. The further ice-water quenching has no effect on the morphologies of TiO_2 nanoparticles.

Table 1. Rutile Relative Contents in the NA-TiO_2, NV-TiO_2, and QV-TiO_2 Samples

annealed temperature (°C)	NA-TiO_2 (%)	NV-TiO_2 (%)	QV-TiO_2 (%)
500	20.7	41.2	39.5
600	30.7	92.5	92.8
700	80.2	100	100
800	100	100	100

3.3. UV−Vis Spectroscopy, EPR, and XPS Analysis. Figure 5A−D shows the UV−vis diffusion spectra of NA-TiO_2, NV-TiO_2, and QV-TiO_2 after annealing at 500, 600, 700, and 800 °C, respectively. TiO_2 belongs to indirect transition semiconductors, with the product of absorption coefficients above the absorption edge and the photon energy being proportional to the root-square of photoenergies. The Tauc plots of these samples are shown in the insets of these figures, based on which the band gap width (E_g) was determined by extrapolation. It can be seen that the E_g values of the different samples are 2.92∼2. 95 eV, closing to the theoretical value of the rutile phase. The vacuum-sealed annealing and further ice-water quenching do not have an effect on the E_g values.

Although the E_g value is not changed, the vacuum-sealed annealing has a clear effect on the band-tail absorption for all annealing temperatures. It can be seen that the NA-TiO_2 samples exhibit an exponential band-tail absorption below the adsorption edge;[39] this was however not seen in the absorption spectra of the NV-TiO_2 and QV-TiO_2 samples, independent of crystalline phases. The NA-TiO_2 samples are shallowly yellow in color, while the NV-TiO_2 and QV-TiO_2 samples are pale-white and shallow-blue, respectively. When the annealing temperature was 700 °C, Figure 5C shows that NV-TiO_2 shows a clear wide absorption at the wavelengths longer than 500 nm; this absorption further increases when the temperature was 800 °C (Figure 5D). Moreover, it can also be seen that the wide absorption can be enhanced by ice-water quenching (QV-700 and QV-800). The exponential-tail absorptions in the spectra of NA-TiO_2 arise from the electron localization at oxygen vacancy sties,[40] and the visible−NIR featureless wide-range absorptions in the spectra of NV-TiO_2 and QV-TiO_2 samples are attributed to the electron localization at lattice Ti sites.[18] Therefore, the above result shows that the vacuum-sealed annealing process can change the electron localization from oxygen vacancies to Ti sites. It seems that, although the further ice-water quenching can increase the defect concentration, the electron localization has not been altered.

The EPR spectra of NA-TiO_2, NV-TiO_2, and QV-TiO_2 samples after annealing at 800 °C were recorded to show electron localization, as shown in Figure 6A. The g values at 1.98

https://doi.org/10.1021/acsomega.2c04695
ACS Omega 2022, 7, 43710−43718

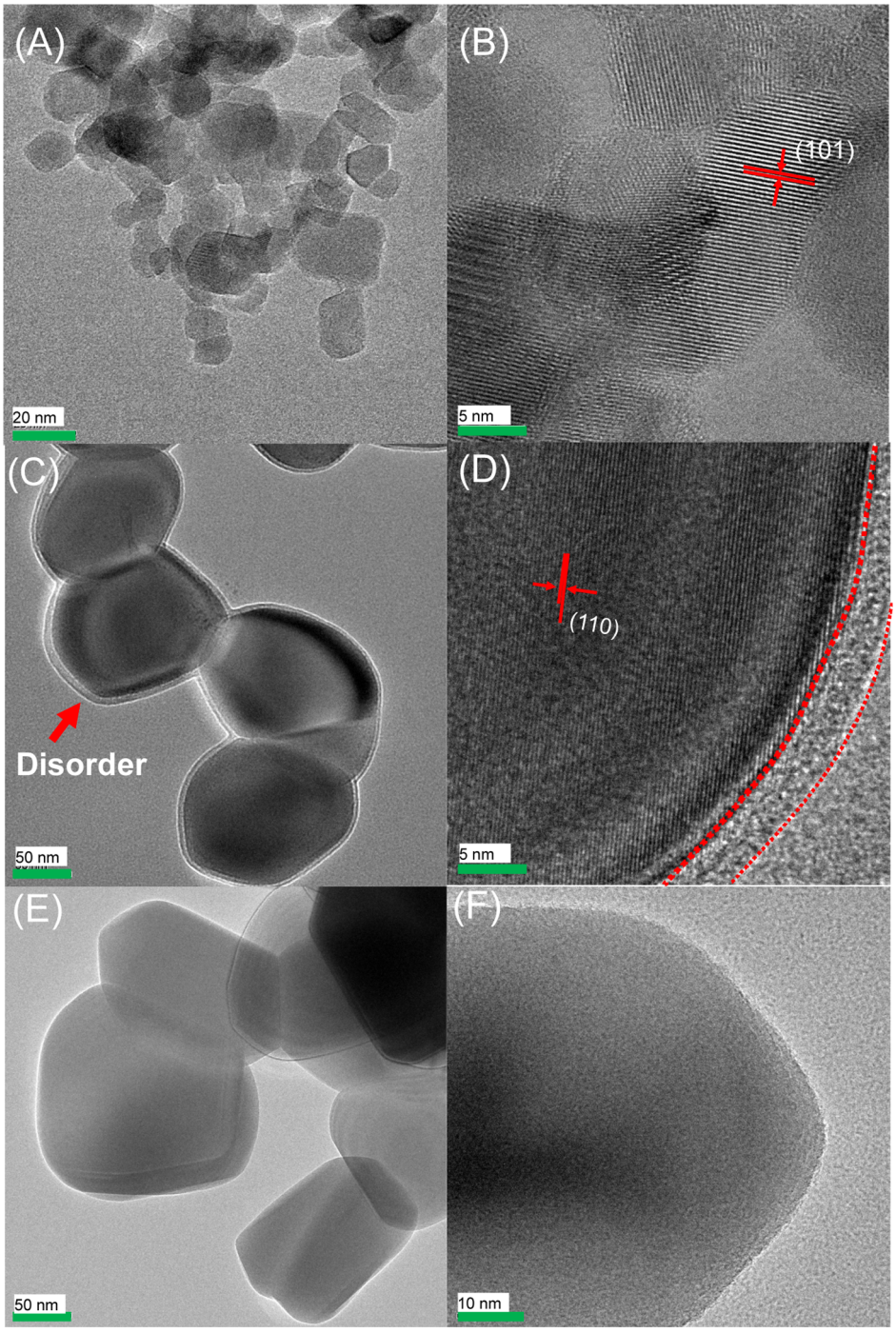

Figure 4. (A,B) TEM and HR-TEM images of P25; (C,D) TEM and HR-TEM images of NV-TiO_2-700; and (E,F) TEM and HR-TEM images of NV-TiO_2-800.

and 2.003 are ascribed to Ti^{3+} and O_2^-, respectively.[41] It seems that the Ti^{3+} signal shows a slight increase for the ice-water-quenched vacuum-sealed sample; this also agrees well with the UV−vis spectra. NV-TiO_2 does not present increased Ti^{3+} signals due to the low amount as compared to NA-TiO_2. The surface chemical compositions of NA-TiO_2-800 and QV-TiO_2-800 were also checked by XPS. Figure 6B,C shows the O 1s and Ti 2p core-level spectra, as well as the Gaussian fitted lines. The O 1s spectra contain two peaks at 530.9 and 530.2 eV, respectively; they are ascribed to lattice oxygens and surface hydroxyl groups (OH^-), respectively.[30] The Gaussian fitting shows that the vacuum-sealed annealing results in a decrease in the surface hydroxyl content because of the isolation of TiO_2 from air. It can also be seen from Figure 6C that the Ti 2p spectrum of QV-TiO_2 shifts to a low binding energy as compared to NA-TiO_2, indicating that more defects are generated by vacuum-sealed annealing and quenching; this is in accordance with the UV−vis and EPR analysis.

3.4. Positron Annihilation Study. Positron annihilation was used to analyze oxygen defects in the samples after annealing at 800 °C because of more defects in this sample. The positron decay spectra can be fitted with two characteristic lifetimes. The longer lifetime component (τ_2) arises from the positron trapped by larger defects such as oxygen vacancy clusters (i.e., dimers,

https://doi.org/10.1021/acsomega.2c04695
ACS Omega 2022, 7, 43710−43718

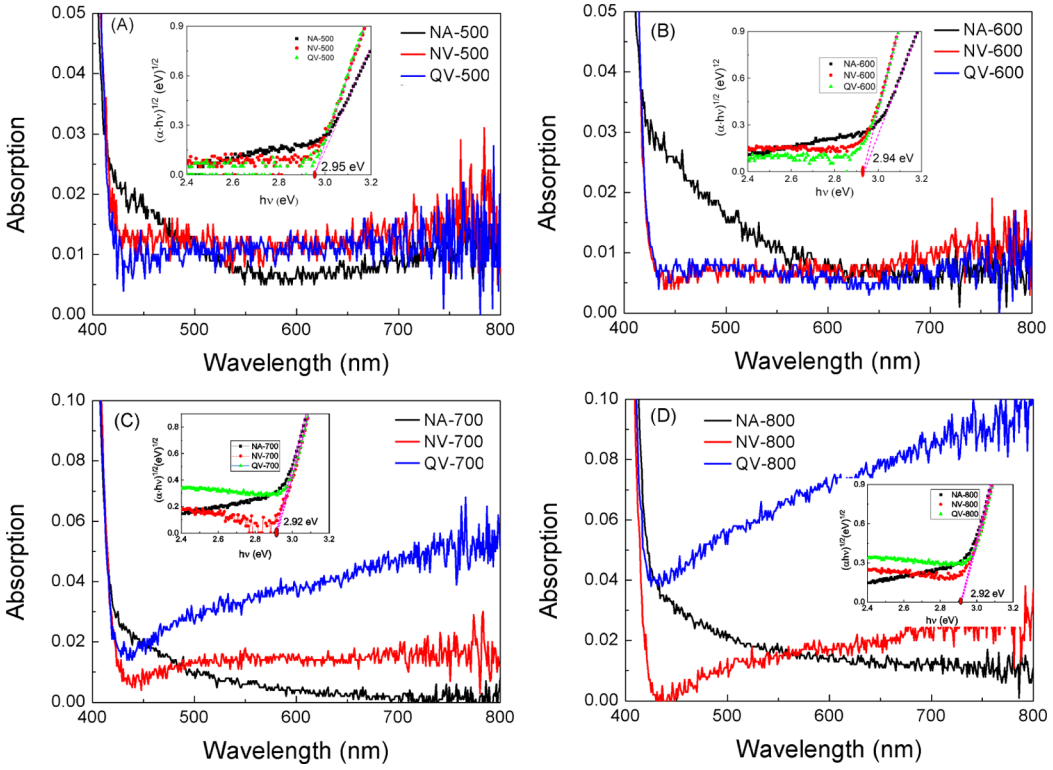

Figure 5. UV−vis diffusion spectra of the NA-TiO_2, NV-TiO_2, and QV-TiO_2 samples after annealing at 500 (A), 600 (B), 700 (C), and 800 °C (D), respectively (the insets show the Tauc plots for obtaining the forbidden band gaps).

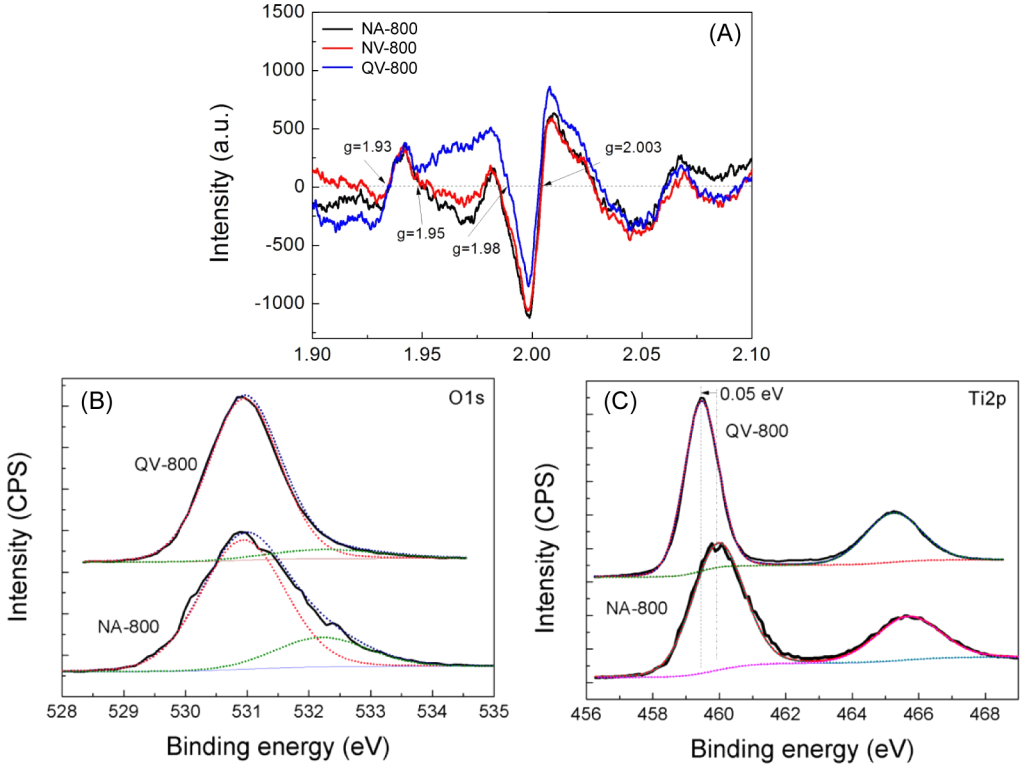

Figure 6. (A) EPR spectra of NA-TiO_2, NV-TiO_2, and QV-TiO_2 after annealing at 800 °C; (B) O 1s high-resolution core-level XPS spectra of NA-TiO_2 and NV-TiO_2 after annealing at 800 °C; and (C) Ti 2p high-resolution core-level XPS spectra of NA-TiO_2 and NV-TiO_2 after annealing at 800 °C.

trimers, or larger).[26,42] Generally, the shorter lifetime components (τ_1) are attributed to the free annihilation of positrons in defect-free crystals or the bulk single-electron-trapped oxygen vacancies that possess one single electron.[42] We thus attribute the shorter one (τ_1) to the positron annihilation at the bulk oxygen vacancies or Ti^{3+} sites. Because the amount of

https://doi.org/10.1021/acsomega.2c04695
ACS Omega 2022, 7, 43710−43718

surface oxygen vacancies is abundant, which can gather to form dimer, trimer, or clusters, the longer one (τ_2) corresponds to the position lifetime annihilated in surface oxygen defects. As shown in Table 2, the ratio of I_2 (surface oxygen defect percentage) to I_1 (bulk oxygen defect percentage) (I_2/I_1) of NA-TiO_2, NV-TiO_2, and QV-TiO_2 decreases; this indicates that the ratio of bulk to surface defects is increased by vacuum-sealed annealing, and the ice-water quenching can further increase the bulk defect content by 6%. Therefore, the positron annihilation results also show that the vacuum-sealed annealing and ice-water quenching change the defect distribution defects and electron localization at them; this is also in good accordance with the above UV−vis spectroscopy analysis.

Table 2. Positron Annihilation Lifetimes and Relative Percentages Relating to Bulk and Surface Defects for the Different Samples Annealed at 800 °C

sample	τ_1 (ps)[a]	τ_2 (ps)[b]	I_1 (%)[c]	I_2 (%)[d]	I_2/I_1
NA-TiO_2	156	269	25.7	74.3	2.89
NV-TiO_2	166	297	45.1	54.9	1.21
QV-TiO_2	182	309	46.7	53.3	1.14

[a]Position annihilation lifetime relating to bulk oxygen defects. [b]Position annihilation lifetime relating to surface oxygen defects. [c]Relative percentage of bulk oxygen defects. [d]Relative percentage of surface oxygen defects.

In summary, in addition to crystallinity and morphologies, the vacuum-sealed annealing and ice-water quenching can affect the defect and electron localization states; this might connect with the oxygen vacancies that donate excess electrons in the TiO_2 lattice. The electron localization at different sites can form different intermediate gap states. The electron localization sites (oxygen vacancies or Ti sites) also depend on the preparation condition. The electrons mainly trapped at oxygen vacancies for NA-TiO_2, while they become localized at Ti sites for the vacuum-sealed samples. In addition, the further vacuum-sealed annealing can also increase defect concentrations and almost has less effect on their distribution.

3.5. Photocatalytic Acetone Oxidations. When the annealed temperatures were 700 and 800 °C, it can be seen that the obtained TiO_2 materials are inactive because all of the anatase phase TiO_2 is converted to rutile. Therefore, the observed photocatalytic effect should be caused by the anatase phase in the TiO_2 materials. Figure 7 shows the CO_2 evolutions in the dark and under UV light illuminations during acetone photocatalytic oxidations over NA-TiO_2, NV-TiO_2, and QV-TiO_2 annealed at 500 and 600 °C. It can be seen that the vacuum-sealed annealing and the ice-water quenching lead to an apparent decrease in CO_2 evolution rates. As the contents of anatase phase TiO_2 in these samples are different, the photocatalytic CO_2 evolution rates were compared by normalizing to the anatase amounts of NA-TiO_2, as shown in Figure 7C. Independent of quenching or not, it can be seen that the vacuum-sealed annealing can increase the photocatalytic activity of the anatase TiO_2 to some extent. The photocatalytic activity of NV-TiO_2-600 is ~4 times higher than that of NA-TiO_2. However, ice-water quenching leads to the decrease of the activity. Combined with the above analysis, it is considered that

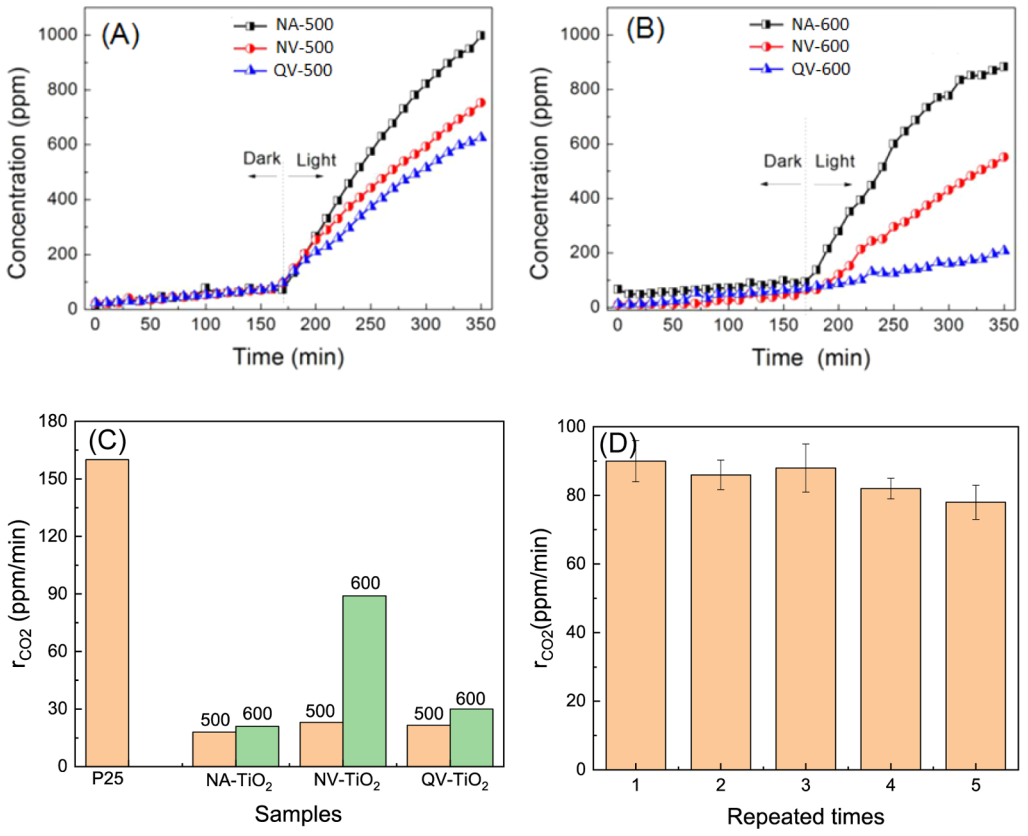

Figure 7. CO_2 evolutions during the photocatalytic acetone oxidations over NA-TiO, NV-TiO_2, and QV-TiO_2 annealed at 500 (A) and 600 °C (B); (C) CO_2 evolution rates of p25 TiO_2 and anatase TiO_2 phase in NA-TiO_2, NV-TiO_2, and QV-TiO_2; and (D) repeated CO_2 evolution rates of the anatase TiO_2 phase in NV-TiO2-600.

https://doi.org/10.1021/acsomega.2c04695
ACS Omega 2022, 7, 43710−43718

the defect amounts and electron localization might be in close connection with the photocatalytic properties, and defect distribution should have less effect on photocatalysis. The vacuum-sealed annealing mainly introduces Ti^{3+} defects, and the ice-water quenching creates more bulk Ti^{3+} in TiO_2. Therefore, introducing a suitable amount of Ti^{3+} defects might be beneficial for photocatalytic acetone oxidations, and more Ti^{3+} states might form recombination centers and decrease the photocatalytic activity. In addition, the photocatalytic activity of commercial P25 was also measured under the same condition for comparison; the initial CO_2 generation rate is shown in Figure 7C. It can be seen that the CO_2 evolution rate of P25 is much higher; the low activity of other samples is attributed to the decrease in the specific surface area and the defect generation caused by annealing. It can be seen from Figure 7D that the anatase phase TiO_2 in NV-TiO_2-600 also shows relatively good stability for photocatalytic acetone oxidation. The apparent photocatalytic activity was decreased by 15% after five times photocatalytic cycles. As no water vapor was introduced during all photocatalytic reactions, it is considered that O_2^- should contribute to the photocatalytic acetone oxidation, which is also verified by the EPR spectrum under UV light illumination that shows the presence of O_2^- signal.

4. CONCLUSIONS

In summary, the vacuum-sealed annealing process has an effect on the crystalline structures, nanoparticle morphologies, and electronic structures of the TiO_2 materials. The anatase-to-rutile phase temperature was decreased by more than 100∼150 °C. The vacuum-sealed annealing process could also create a clear disordered layer around TiO_2 nanoparticles; this results in the decrease of TiO_2 crystallinity. The further ice-water quenching could not lead to more change in the crystalline structure of the vacuum-sealed samples. As compared to the normally obtained samples, it can also be seen that more defects, including oxygen defects and Ti^{3+} states, were generated in TiO_2 by vacuum-sealed annealing; the content of bulk defect was increased, and the electron localization at oxygen defects was altered. The ice-water quenching could lead to a further increase in defect density, and more defects locate in the bulk; it seems that the electron localization was not affected. The photocatalytic activity of the anatase TiO_2 phase was increased by vacuum-sealed annealing; this might be connected with the generated defects and electron localization at Ti sites. Further quenching led to a decrease in activities, possibly because more defects were generated and the recombination is increased.

AUTHOR INFORMATION

Corresponding Author

Baoshun Liu − *State Key Laboratory of Silicate Materials for Architectures, Wuhan University of Technology, Wuhan City, Hubei province 430070, P. R. China;* orcid.org/0000-0001-5564-3685; Phone: +86-13871104906; Email: bshliu@whut.edu.cn

Authors

Liping Wen − *School of Environmental & Biological Engineering, Wuhan Technology and Business University, Wuhan City, Hubei province 430065, P. R. China*

Yao Liu − *School of Environmental & Biological Engineering, Wuhan Technology and Business University, Wuhan City, Hubei province 430065, P. R. China*

Yong Liu − *School of Environmental & Biological Engineering, Wuhan Technology and Business University, Wuhan City, Hubei province 430065, P. R. China*

Yuping Xu − *School of Environmental & Biological Engineering, Wuhan Technology and Business University, Wuhan City, Hubei province 430065, P. R. China*

Complete contact information is available at: https://pubs.acs.org/10.1021/acsomega.2c04695

Notes

The authors declare no competing financial interest.

ACKNOWLEDGMENTS

This work was supported by the Guidance Project of Hubei Provincial Department of Education for Scientific Research (B2020246), the Research Fund for the Doctoral Program of Wuhan Technology and Business University (D2019008), and the Special Fund of Advantageous and Characteristic Disciplines (Group) of Hubei Province. B.L. thanks the National Key Research and Development of China (no. 2017YFE0192600) and the National Natural Science Foundation of China (no. 51772230).

REFERENCES

(1) Kayaci, F.; Vempati, S.; Donmez, I.; Biyikli, N.; Uyar, T. Role of Zinc Interstitials and Oxygen Vacancies of ZnO in Photocatalysis: a Bottom-up Approach to Control Defect Density. *Nanoscale* **2014**, *6*, 10224−10234.

(2) Xiong, J.; Di, J.; Xia, J.; Zhu, W.; Li, H. Surface Defect Engineering in 2D Nanomaterials for Photocatalysis. *Adv. Funtc. Mater.* **2018**, *28*, 1801983.

(3) Suriye, K.; Praserthdam, P.; Jongsomjit, B. Control of Ti^{3+} Surface Defect on TiO_2 Nanocrystal Using Various Calcination Atmospheres as the First Step for Surface Defect Creation and its Application in Photocatalysis. *Appl. Surf. Sci.* **2007**, *253*, 3849−3855.

(4) Kong, L.; Wang, C.; Zheng, H.; Zhang, X.; Liu, Y. Defect-Induced Yellow Color in Nb-Doped TiO_2 and Its Impact on Visible-Light Photocatalysis. *J. Phys. Chem. C* **2015**, *119*, 16623−16632.

(5) Wei, W.; Yao, Y.; Zhao, Q.; Xu, Z.; Wang, Q.; Zhang, Z.; Gao, Y. Oxygen Defect-induced Localized Surface Plasmon Resonance at the WO_{3-x} Quantum Dot/silver Nanowire Interface: SERS and Photocatalysis. *Nanoscale* **2019**, *11*, 5535−5547.

(6) Shi, J.; Cui, H.; Liang, Z.; Lu, X.; Tong, Y.; Su, C.; Liu, H. The Roles of Defect States in Photoelectric and Photocatalytic Processes for $Zn_xCd_{1-x}S$. *Energy Environ. Sci.* **2011**, *4*, 466−470.

(7) Liu, D.; Li, H.; Gao, R.; Zhao, Q.; Yang, Z.; Gao, X.; Wang, Z.; Zhang, F.; Wu, W. Enhanced Visible Light Photoelectrocatalytic Degradation of Tetracycline Hydrochloride by I and P Co-doped TiO_2 Photoelectrode. *J. Hazard. Mater.* **2021**, *406*, 124309.

(8) Liu, D.; Li, C.; Zhao, C.; Zhao, Q.; Niu, T.; Pan, L.; Xu, P.; Zhang, F.; Wu, W.; Ni, T. Facile Synthesis of Three-dimensional Hollow Porous Carbon Doped Polymeric Carbon Nitride with Highly Efficient Photocatalytic Performance. *Chem. Eng. J.* **2022**, *438*, 135623.

(9) Nowotny, M. K.; Sheppard, L. R.; Bak, T.; Nowotny, J. Defect Chemistry of Titanium Dioxide. Application of Defect Engineering in Processing of TiO_2-Based Photocatalysts. *J. Phys. Chem. C* **2008**, *112*, 5275−5300.

(10) Wan, J.; Chen, W.; Jia, C.; Zheng, L.; Dong, J.; Zheng, X.; Wang, Y.; Yan, W.; Chen, C.; Peng, Q.; Wang, D.; Li, Y. Defect Effects on TiO_2 Nanosheets: Stabilizing Single Atomic Site Au and Promoting Catalytic Properties. *Adv. Mater.* **2018**, *30*, 1705369.

(11) Wei, T.; Zhu, Y.; An, X.; Liu, L.; Cao, X.; Liu, H.; Qu, J. Defect Modulation of Z-Scheme TiO_2/Cu_2O Photocatalysts for Durable Water Splitting. *ACS Catal.* **2019**, *9*, 8346−8354.

(12) Ji, Z.; Wu, J.; Jia, T.; Peng, C.; Xiao, Y.; Liu, Z.; Liu, Q.; Fan, Y.; Han, J.; Hao, L. In-situ Growth of TiO_2 Phase Junction Nanorods with

Ti^{3+} and Oxygen Vacancies to Enhance Photocatalytic Activity. *Mater. Res. Bull.* **2021**, *140*, 111291.
(13) Chen, S.; Xiao, Y.; Wang, Y.; Hu, Z.; Zhao, H.; Xie, W. A Facile Approach to Prepare Black TiO_2 with Oxygen Vacancy for Enhancing Photocatalytic Activity. *Nanomaterials* **2018**, *8*, 245.
(14) Kong, L.; Zhang, X.; Wang, C.; Wan, F.; Li, L. Synergic Effects of Cu_xO Electron Transfer Co-catalyst and Valence Band Edge Control over TiO_2 for Efficient Visible-light Photocatalysis. *Chin. J. Catal.* **2017**, *38*, 2120−2131.
(15) Zhao, Y.; Zhao, Y.; Shi, R.; Wang, B.; Waterhouse, G. I. N.; Wu, L.; Tung, C.; Zhang, T. Tuning Oxygen Vacancies in Ultrathin TiO_2 Nanosheets to Boost Photocatalytic Nitrogen Fixation up to 700 nm. *Adv. Mater.* **2019**, *31*, 1806482.
(16) Shen, X.; Dong, G.; Wang, L.; Ye, L.; Sun, J. Enhancing Photocatalytic Activity of NO Removal through an In Situ Control of Oxygen Vacancies in Growth of TiO_2. *Adv. Mater. Interfaces* **2019**, *6*, 1901032.
(17) Dagdeviren, O. E.; Glass, D.; Sapienza, R.; Cortés, E.; Maier, S. A.; Parkin, I. P.; Grütter, P.; Quesada-Cabrera, R. The Effect of Photoinduced Surface Oxygen Vacancies on the Charge Carrier Dynamics in TiO_2 Films. *Nano Lett.* **2021**, *21*, 8348−8354.
(18) Liu, B.; Zhao, X.; Yu, J.; Parkin, I. P.; Fujishima, A.; Nakata, K. Intrinsic Intermediate Gap States of TiO_2 Materials and Their Roles in Charge Carrier Kinetics. *J. Photochem. Photobiol., C* **2019**, *39*, 1−57.
(19) Liu, B.; Wang, J.; Yang, J.; Zhao, X. Charge Carrier Interfacial Transfer Pathways from TiO_2 and Au/TiO_2 Nanorod Arrays to Electrolyte and the Association with Photocatalysis. *Appl. Surf. Sci.* **2019**, *464*, 367−375.
(20) Liu, B.; Yang, J.; Wang, J.; Zhao, X.; Nakata, K. High Sub-band Gap Response of TiO_2 Nanorod Arrays for Visible Photoelectrochemical Water Oxidation. *Appl. Surf. Sci.* **2019**, *465*, 192−200.
(21) Qian, R.; Zong, H.; Schneider, J.; Zhou, G.; Zhao, T.; Li, Y.; Yang, J.; Bahnemann, D. W.; Pan, J. H. Charge Carrier Trapping, Recombination and Transfer uring TiO_2 Photocatalysis: An Overview. *Catal. Today* **2019**, *335*, 78−90.
(22) Feng, X.; Wang, P.; Hou, J.; Qian, J.; Ao, Y.; Wang, C. Significantly Enhanced Visible Light Photocatalytic Efficiency of Phosphorus Doped TiO_2 with Surface Oxygen Vacancies for Ciprofloxacin Degradation: Synergistic Effect and Intermediates Analysis. *J. Hazard. Mater.* **2018**, *351*, 196−205.
(23) Xie, H.; Li, N.; Chen, X.; Jiang, J.; Zhao, X. Surface Oxygen Vacancies Promoted Photodegradation of Benzene on TiO_2 Fiml. *Appl. Surf. Sci.* **2020**, *511*, 145597.
(24) Li, J.; Weng, B.; Cai, S.; Chen, J.; Jia, H.; Xu, Y. Efficient Promotion of Charge Transfer and Separation in Hydrogenated TiO_2/WO_3 with Rich Surface-oxygen-vacancies for Photodecomposition of Gaseous Toluene. *J. Hazard. Mater.* **2018**, *342*, 661−669.
(25) Hou, L.; Zhang, M.; Guan, Z.; Li, Q.; Yang, J. Effect of Annealing Ambience on the Formation of Surface/bulk oxygen Vacancies in TiO_2 for Photocatalytic Hydrogen Evolution. *Appl. Surf. Sci.* **2018**, *428*, 640−647.
(26) Kong, M.; Li, Y.; Chen, X.; Tian, T.; Fang, P.; Zheng, F.; Zhao, X. Tuning the Relative Concentration Ratio of Bulk Defects to Surface Defects in TiO_2 Nanocrystals Leads to High Photocatalytic Efficiency. *J. Am. Chem. Soc.* **2011**, *133*, 16414−16417.
(27) Xiu, Z.; Guo, M.; Zhao, T.; Pan, K.; Xing, Z.; Li, Z.; Zhou, W. Recent Advances in Ti^{3+} self-doped Nanostructured TiO_2 Visible Light Photocatalysts for Environmental and Energy Applications. *Chem. Eng. J.* **2020**, *382*, 123011.
(28) Wang, G.; Zheng, J.; Bi, H.; Wang, S.; Wang, J.; Sun, J.; Guo, Y.; Wang, C. Ti^{3+} Self-Doping in Bulk of Rutile TiO_2 for Enhanced Photocatalysis. *Scripta Mater.* **2019**, *162*, 28−32.
(29) Wang, X.; Li, Y.; Liu, X.; Gao, S.; Huang, B.; Dai, Y. Preparation of Ti^{3+} Self-doped TiO_2 Nanoparticles and Their Visible Light Photocatalytic Activity. *Chin. J. Catal.* **2015**, *36*, 389−399.
(30) Xing, M.; Fang, W.; Nasir, M.; Ma, Y.; Zhang, J.; Anpo, M. Self-doped Ti^{3+}-enhanced TiO_2 Nanoparticles with a High-performance Photocatalysis. *J. Catal.* **2013**, *297*, 236−243.
(31) Yu, X.; Kim, B.; Kim, K. K. Highly Enhanced Photoactivity of Anatase TiO_2 Nanocrystals by Controlled Hydrogenation-Induced Surface Defects. *ACS Catal.* **2013**, *3*, 2479−2486.
(32) Yu, F.; Wang, C.; Li, Y.; Ma, H.; Wang, R.; Liu, Y.; Suzuki, N.; Terashima, C.; Ohtani, B.; Ochiai, T.; Fujishima, A.; Zhang, X. Enhanced Solar Photothermal Catalysis over Solution Plasma Activated TiO_2. *Adv. Sci.* **2020**, *7*, 2000204.
(33) Yu, F.; Wang, C.; Ma, H.; Song, M.; Li, D.; Li, Y.; Li, S.; Zhang, X.; Liu, Y. Revisiting Pt/TiO_2 Photocatalysts for Thermally-assisted Photocatalytic Reduction of CO_2. *Nanoscale* **2020**, *12*, 7000−7010.
(34) Carter, E.; Carley, A. F.; Murphy, D. M. Evidence for O_2^- Radical Stabilization at Surface Oxygen Vacancies on Polycrystalline TiO_2. *J. Phys. Chem. C* **2007**, *111*, 10630−10638.
(35) Karmakar, P.; Liu, G. F.; Yarmoff, J. A. Sputtering-induced Vacancy Cluster Formation on TiO_2(110). *Phys. Rev. B: Condens. Matter Mater. Phys.* **2007**, *76*, 193410.
(36) Liu, B.; Cheng, K.; Nie, S.; Zhao, X.; Yu, H.; Yu, J.; Fujishima, A.; Nakata, K. Ice−Water Quenching Induced Ti^{3+} Self-doped TiO_2 with Surface Lattice Distortion and the Increased Photocatalytic Activity. *J. Phys. Chem. C* **2017**, *121*, 19836−19848.
(37) Liu, B.; Yan, L.; Wang, J. Liquid N_2 Quenching Induced Oxygen Defects and Surface Distortion in TiO_2 and the Effect on the Photocatalysis of Methylene Blue and Acetone. *Appl. Surf. Sci.* **2019**, *494*, 266−274.
(38) Zhang, J.; Li, M.; Feng, Z.; Chen, J.; Li, C. UV Raman Spectroscopic Study on TiO_2. I. Phase Transformation at the Surface and in the Bulk. *J. Phys. Chem. B* **2006**, *110*, 927−935.
(39) Chen, H.; Dawson, J. A. Nature of Nitrogen-Doped Anatase TiO_2 and the Origin of Its Visible-Light Activity. *J. Phys. Chem. C* **2015**, *119*, 15890−15895.
(40) Sekiya, T.; Yagisawa, T.; Kamiya, N.; Das Mulmi, M. D.; Kurita, S.; Murakami, Y.; Kodaira, T. Defects in Anatase TiO_2 Single Crystal Controlled by Heat Treatments. *J. Phys. Soc. Jpn.* **2004**, *73*, 703−710.
(41) Sham, T. K.; Lazarus, M. S. X-ray Photoelectron Spectroscopy (XPS) Studies of Clean and Hydrated TiO_2 (rutile) Surfaces. *Chem. Phys. Lett.* **1979**, *68*, 426−432.
(42) Li, Q.; Mao, W.; Zhou, Y.; Yang, C.; Liu, Y.; He, C. Defects Evolution and Their impacts on Conductivity of Indium Tin Oxide Thin Films upon Thermal Treatment. *J. Appl. Phys.* **2015**, *118*, 025304.

https://doi.org/10.1021/acsomega.2c04695
ACS Omega 2022, 7, 43710−43718